J. Asiat. Soc. Bangladesh, Sci. **51**(1): 19-38, June 2025
DOI: http://doi.org/10:3329/jasbs.v51i1.82788

SPATIOTEMPORAL CHANGES OF LAND USE, LAND SURFACE TEMPERATURE AND URBAN HEAT ISLAND IN BOGURA DISTRICT USING MULTISPECTRAL SATELLITE IMAGES

MD. RASHIDUL ISLAM, MD. BODRUDDOZA MIA*, MD. NASIF JAMIL, MASUMA CHOWDHURY AND ASM WOOBAIDULLAH
Geoinformatics Laboratory, Department of Geology, Faculty of Earth and Environmental Sciences, University of Dhaka, Dhaka-1000, Bangladesh

Abstract

This study presents an in-depth analysis of the spatiotemporal changes in land use/land cover (LULC) land surface temperature (LST) and urban heat islands (UHI) in Bogura District, with a focus on Bogura Municipality, utilizing multispectral satellite images from 1993 to 2023. The LULC of supervised classification identified significant shifts, including a sharp expansion of settlement areas, particularly by 2023, and a notable increase in vegetation cover, reflecting improved vegetation health. However, agricultural and fallow lands have shown a marked decline, especially post-2000, suggesting shifts in land use or a reduction in vegetation density. Water bodies have gradually decreased in areas, likely due to land conversion or the drying up of sources. The normalized difference vegetation index (NDVI) analysis corroborates these findings, highlighting fluctuations in vegetation health and coverage. Concurrently, LST analysis reveals an increase in higher temperature categories, closely linked to urbanization and the formation of urban heat islands (UHIs). The expansion of settlement areas has intensified the UHI effect, where urban zones exhibit significantly higher temperatures compared to surrounding rural areas. Additionally, areas of low temperature have expanded, indicating changes in land surface characteristics. The data underscores the dynamic nature of land use changes over the three-decade period, with urbanization and land cover alterations significantly impacting both vegetation and surface temperatures in the region. The study provides a framework for creating plans to counteract the negative effects of climate change, especially the UHI effect, and to direct sustainable urban planning.

Key words: Landuse, Land Surface Temperature, Urban Heat Island, Bogura District, Landsat image.

Introduction

Urbanization and environmental change are profoundly interconnected, affecting ecosystems, biodiversity, and local climates. Urban expansion's fast alteration of land use and land cover (LULC) has a profound effect on ecosystems, biodiversity, and the local and regional climate (Luck and Wu, 2002). The rapid urbanization in Bogura District has

*Corresponding author: bodruddoza@du.ac.bd

led to significant land use and land cover (LULC) changes over the past thirty years. Remote sensing techniques have a vital role in identifying and controlling different meteorological and environmental occurrences (Borges *et al.,* 2016). Utilizing satellite imagery from Landsat 5, 7, 8, and 9, this study investigates how these changes have influenced land surface temperature (LST) and contributed to the formation of urban heat islands (UHI). The Mono-window approach is a simplified method for calculating LST that only requires a small number of specific meteorological data (Jie *et al.,* 2008, Ding and Shi, 2013). Several recent studies have utilized satellite data to examine the impacts of Land Use and Land Cover Change (LULC) on Land Surface Temperature (LST) (Ahmed *et al.,* 2013; Zhang and He 2013). Previous studies highlight the impact of urban expansion on ecosystems and climate, noting that rising LST leads to reduced plant cover and increased heat island effects (Ramachandra *et al.,* 2012). Socio-economic advancement linked with urbanization often results in significant and lasting LULC changes. These changes exhaust agricultural lands, threaten biodiversity, and alter water resources, thereby affecting local and regional climates. The Bogura District, with its rapid population growth and extensive agricultural expansion, faces numerous environmental challenges exacerbated by climate change. This study aims to address these issues by monitoring biophysical data and analyzing their temporal and spatial relationships.

Despite the critical nature of LST and UHI phenomena, accurate assessments of land use patterns remain underexplored. According to (Weng *et al.,* 2004), there is a positive correlation between Land Surface Temperature (LST) and the percentage of impermeable surfaces, while there is a negative correlation between LST and the percentage of green vegetation. Land surface temperature is a crucial parameter in land surface modeling, influenced by various environmental factors and measurable through satellite thermal infrared sensors (Kustas and Norman, 1996). This technology employs satellite and airplane platforms, providing novel prospects for investigating the occurrence of HIs (Voogt and Oke, 2003). Understanding the formation and growth of UHIs, areas with significantly higher temperatures due to urbanization, is essential for developing mitigation strategies (Xie and Zhou, 2015). By selecting appropriate satellite images and utilizing remote sensing techniques, this study aims to enhance our understanding of LULC dynamics and UHI development in Bogura District. The findings will be crucial for mitigating socio-economic risks, such as drought, flooding, and biodiversity loss, which are aggravated by climate change. Studies in various regions, including Dhaka and Gazipur in Bangladesh, have shown significant LULC changes affecting LST. However, the Bogura District lacks comprehensive studies on LULC and LST changes. This study

aims to analyze LULC changes and their relation to UHI development in Bogura District using multi-spectral satellite imagery. Various Landsat TM/ETM+/TIRS sensor's images are used to study the urban heat island (UHI) effect.

Study area

The study area is Bogura District, and it is located in the northwestern part of Bangladesh under Rajshahi Division (Fig. 1). The latitude of Bogura District is 24°51`N -24°85`N and longitude is 89°22`E- 89°36`E.The area covers 2899 square kilometers (District Statistics 2011: Bogura). The climate of the Bogura District is intense tropical monsoon which consists of two main seasons which are dry season (November to March) and rainy season (June to October). The average precipitation rate of the area is 1760 mm per year (BMD, 2021). January is the coldest and April is the warmest month in the study area.The population of the area is 38,15,192 and the average density is 1,316/km^2 (BBS, 2022).

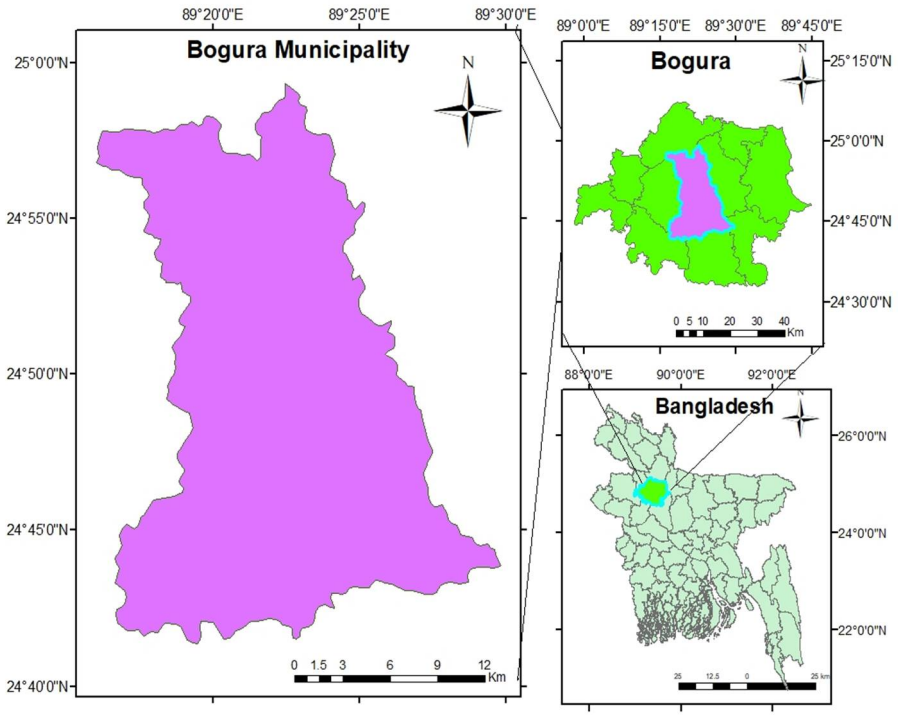

Fig. 1. Location map of the study area.

Materials and Methods

The study is conducted with Landsat satellite images using supervised classification and various indices approaches to quantify the spatiotemporal changes of landuse, and algorithm retrieved LST and UHI of the Bogura district in Bangladesh (Fig. 2).

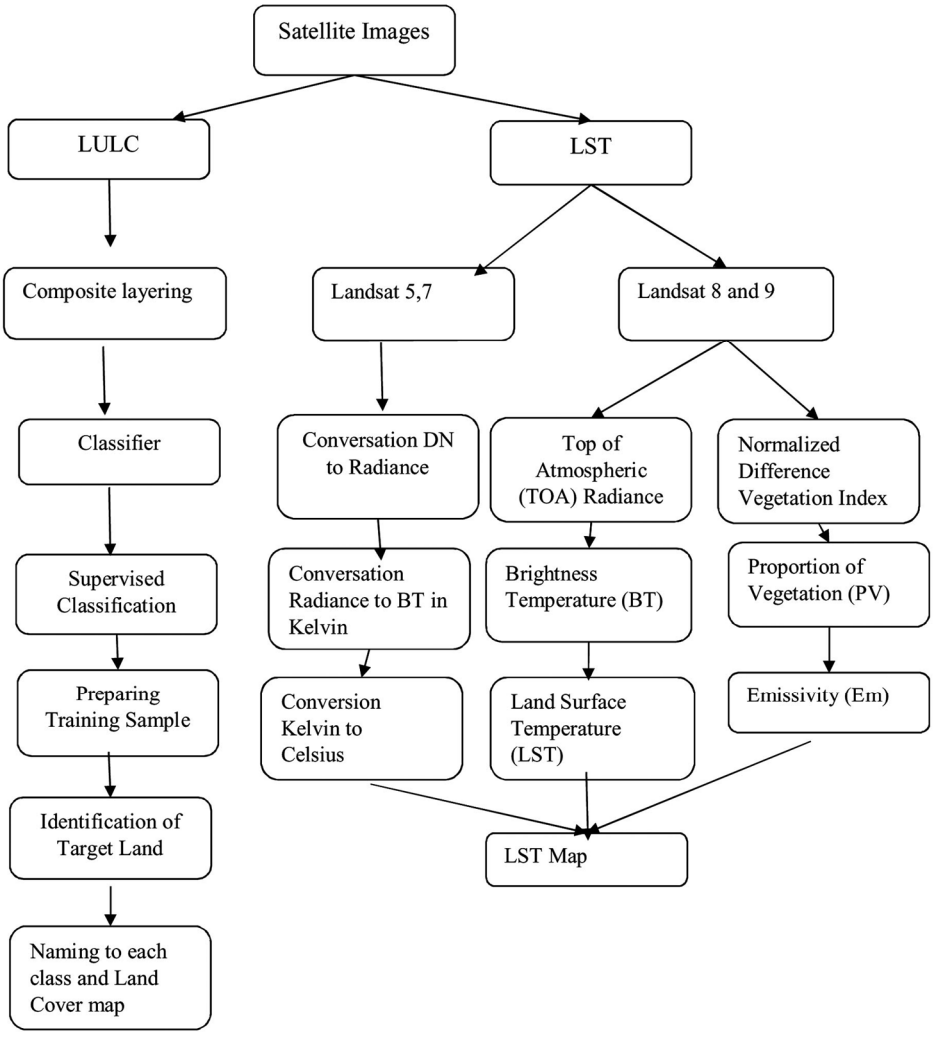

Fig. 2. Methodological flow chart of the study.

Satellite Images

Satellite imagery is often utilized to study the 'heat island effect' in metropolitan areas (Walawender *et al.*, 2014). To conduct this study, we obtained six sets of Landsat images in GeoTIFF format for free from the United States Geological Survey (USGS) collection, which is available at (https://earthexplorer.usgs.gov/). The images, which cover the Bogura District in the years 1993, 2000, 2005, 2010, 2017, and 2023, were chosen from three distinct path and row combinations to cover the full research region. These pictures were georeferenced using the Universal Transverse Mercator (UTM) zone 45N coordinate system, with reference to the World Geodetic System (WGS) 1984 datum, and taken during daylight hours. Due to the scarcity of images with less than 10% cloud cover along the required pathways and rows, there were random pauses between collections. (Table 1) summarizes the data gathered from the United States Geological Survey.

Table 1. Landsat Images Used in the Study.

Year	Sensor Platform	Acquisition Date	Resolution
1993	Landsat 5 TM	08-12-1993	30 m
2000	Landsat 7 ETM+	17-12-2000	
2005	Landsat 5 TM	07-11-2005	
2010	Landsat 5 TM	05-11-2010	
2017	Landsat 8 OLI	08-11-2017	
2023	Landsat 9 OLI	01-11-2023	

Methodology

Image Pre-Processing

This study utilized Landsat level-1 data from USGS Earth Explorer, specifically images from 1993, 2000, 2005, 2010, 2017, and 2023. These images underwent geometric correction to address distortions but often displayed radiometric anomalies due to atmospheric transparency issues, solar radiation variations, and scanning equipment flaws, necessitating radiometric correction for accurate representation.

Radiometric Correction

Radiometric correction is essential for comparing datasets over time, as it mitigates spectral property influences (Paolini *et al.*, 2006). This process involves calibrating pixel values, transforming the sensor's Digital Numbers (DN) into measurements like radiance, reflectance, or brightness temperature. Using sensor-specific metadata, the DN values are

converted into top of the atmosphere (TOA) reflectance and at-sensor radiance, with atmospheric correction achieved through the dark object subtraction method.

Layer Stack, Mosaic, and Subset

After image collection, the bands from the sensors were merged using layer stacking, requiring uniform spatial resolution. Bands that are neither panchromatic nor thermal were combined to enhance land feature distinction. The study area, defined by three images from distinct WRS path and row combinations, was processed using mosaic technique to create a cohesive image. The region of interest was selected and extracted using the subset method, and the research area was partitioned for further analysis.

Conversion of Digital Number (DN) to Radiance

The main procedure for standardizing picture data from various sensors and platforms involves converting DN values to Spectral Radiance, enabling consistent radiometric measurements. Familiarity with the initial scaling coefficients is necessary for this transformation. The spectral radiance (Lλ) has been computed using the equation specified by Zanter (2016).

$$L_\lambda = M_L * Q_{cal} + A_L \quad (1)$$

Where,

L_λ = Spectral radiance (W/ (m^2 * sr * μm))

M_L = Radiance multiplicative scaling factor for the band.

A_L = Radiance additive scaling factor for the band.

Q_{cal} = Pixel value in DN

To proceed with extra processing, it is necessary to convert the digital numbers (DN) to radiance for bands 2, 3, and 4 of the Landsat TM and ETM+ sensors in the years 1993, 2000, 2005, and 2010. To accomplish this, the radiance multiplicative and additive scaling factors for band 2, 3, and 4 of the corresponding images are acquired from the Landsat metadata files that accompany the downloaded images (Table 2).

Table 2. Parameters Used for DN to Radiance conversion.

Year	Sensor	Band No.	Rad. Mul. Scaling Factor (M_L)	Rad. Add. Scaling Factor (A_L)
1993	Landsat-5	2	1.3222	-4.16220
		3	1.0440	-2.21398
		4	0.87602	-2.38602
2000	Landsat 7	2	0.79882	-7.19882
		3	0.62165	-5.62165
		4	0.63976	-5.73976
2005	Landsat-5	2	1.32654	-4.16220
		3	0.72356	-2.62354
		4	0.63976	-5.65165
2010	Landsat-5	2	0.79882	-2.38602
		3	1.05644	-4.62165
		4	0.76543	-3.62165

Conversion of Radiance to TOA Reflectance

To create clear Landsat landscapes, spectral radiation can be converted into reflectance at the planetary or top of atmosphere (TOA) level. Converting photographs offers two advantages when comparing images captured by different sensors. The cosine effect can be utilized to minimize the influence of shifting solar zenith angles caused by variances in data gathering time. Moreover, the fluctuations in solar radiation outside the Earth's atmosphere caused by differences in spectral bands can also be modified. The radiance of the selected bands from the previous phase has been converted into images, which were then used to calculate reflectance. The calculation of the total reflectance from the Earth's surface and atmosphere for the years 1993, 2000, 2005, and 2010 has been conducted using Landsat TM and ETM+ data. The equation used for this calculation is the one supplied by Irish (2000).

$$Q_p = \frac{\pi d^2 L_\gamma}{ESUN_\gamma \cos\theta_s} \quad (2)$$

Where, ρ_p = Planetary Reflectance, L_γ = Spectral Radiance at the sensor's aperture

d = Earth-Sun distance in astronomical units, $ESUN_\gamma$ = Mean solar exoatmospheric irradiance, θ_s = Solar zenith angle in degrees

The solar zenith angle can be determined by subtracting the solar elevation angle, as indicated in the metadata file, from 90 degrees. Additionally, the mean solar exo-atmospheric irradiance (ESUNγ) and the Earth-Sun distance (d) are used in the radiometric correction process to account for variations in solar energy received at the Earth's surface derived using the Julian Calendar, are respectively provided in (Table 3 and Table 4).

Table 3. Solar irradiance for landsat 5(TM) and landsat 7(ETM+).

Band	Landsat 5 (TM) ($W/m^2*\mu m$)	Landsat 7 (ETM^+) ($W/m^2*\mu m$)
1	1957	1970
2	1826	1842
3	1554	1547
4	1036	1044
5	215.0	225.7
7	80.67	82.06
8	-	1369

Table 4. Parameters used for radiance to reflectance conversion.

Year (Landsat sensor)	WRS Path and Row	Earth-Sun distance in astronomical units (d)	Solar zenith angle in degrees (θ_s)	Mean solar exo-atmospheric irradiance ($ESUN_\gamma$)
1993 (TM)	138,42	0.99280	90 - 41.54147541	1826 (Band 2)
	138,43	0.99280	90 - 42.51407377	1554 (Band 3)
	139,42	0.99527	90 - 43.89935287	1036 (Band 4)
2000 (ETM+)	138,42	0.98724	90 - 38.81661247	1842 (Band 2)
	138,43	0.98724	90 - 39.97976610	1547(Band 3)
	139,42	0.98409	90 - 35.19818820	1044(Band 4)
2005 (TM)	139,88	0.98724	90 - 41.36576562	1825 (Band 2)
	138,43	0.99432	90 - 40.68539244	1554(Band 4)
	138,97	0.9967	90 - 43.23474323	1044(Band 4)
2010 (TM)	139,42	0.98724	90 - 39.78468454	1836 (Band 2)
	133,25	0.99543	90 - 41.64748456	1064(Band 4)
	136,89	0.98423	90 - 42.37835688	1044(Band 4)

Conversion of DN to TOA Reflectance

The process of transforming DN values to TOA for Landsat 8 and 9 images is a simple and efficient one-step procedure. This allows for the convenient conversion of data from 2017 and 2023 into reflectance images using the equation (Zanter, 2016).

$$\rho_\lambda = \frac{M_\rho * Q_{cal} + A_\rho}{\sin(\theta_{SE})} \quad (3)$$

Where, ρ_λ = TOA spectral reflectance.

M_ρ = Reflectance multiplicative scaling factor for the band.

A_ρ = Reflectance additive scaling factor for the band.

Q_{cal} = Pixel value in DN.

θ_{SE} = Local sun elevation angle (provided in degrees in the metadata).

To retrieve the Top of Atmosphere (TOA) reflectance values for bands 3, 4, and 5 of Landsat 8 images from the years 2017 and 2023, the reflectance multiplicative and scaling factor values, along with the local sun elevation angle, are extracted from the Landsat metadata files that accompany the downloaded images (Table 5).

Table 5. Parameters Used for DN to Reflectance Conversion.

Year (Landsat Sensor)	WRS path and row	Sun elevation angle in degrees (θ_{SE})	Reflectance multiplicative scaling factor (M_L)	Reflectance additive scaling factor (A_L)
2017 (OLI/TIRS)	138,42	38.24110398	0.00002	-0.100000
	138,43	39.45762644		
	139,42	40.00261158		
2023 (OLI/TIRS)	138,42	42.87747217		
	138,43	44.07959061		
	139,42	45.36241130		

Accuracy Assessment

To distinguish true land cover changes from potential classification errors, error matrices and per-class accuracy indices were calculated for the year 2023. In this process, 90 stratified random points were generated across the study area for the selected year using Google Earth imagery to determine the actual LULC classes. These verified classes, derived from the reference images, were then utilized to assess per-class accuracy (i.e.,

user's and producer's accuracy). Additionally, overall accuracy and the Kappa coefficient for the year were computed to provide a comprehensive evaluation of the classification performance.

Producer's Accuracy (PA): Measures how well a particular land cover class has been classified, from the perspective of the classifier (or producer). It indicates the probability that a reference pixel (ground truth) is correctly classified in the map.

User's Accuracy (UA): Measures the accuracy from the user's perspective, showing how often the class on the map represents the real-world category.

Both Producer's Accuracy and User's Accuracy are typically reported together, but Overall Accuracy is a combined metric that represents the proportion of correctly classified pixels across all classes.

Normalized Difference Vegetation Index (NDVI) Retrieval

The Normalized Difference Vegetation Index (NDVI) evaluates vegetation by quantifying the difference between near-infrared light, which is strongly reflected by plants, and red light, which is absorbed by plants. The vegetated sections are represented with a higher luminosity, whereas the non-vegetated portions are represented with a lower luminosity. The computation of NDVI can be executed utilizing the equation stated by (Rouse et. al in 1974).

$$\text{NDVI} = \frac{NIR - RED}{NIR + RED} \qquad (4)$$

Where, NIR =Reflectance of Near Infra-red band

RED = Reflectance of Red band

The Normalized Difference Vegetation Index (NDVI) is a quantitative measure that ranges from -1 to +1. Regions with abundant vegetation exhibit positive values close to +1, while places covered by snow, clouds, and bodies of water have lower values near -1. Band 4 of Landsat 5 (TM) and Landsat 7 (ETM+) corresponds to the Near Infrared (NIR) region, while band 3 represents the Red region.

$$\text{NDVI} = \frac{Band\ 4 - Band\ 3}{Band\ 4 + Band\ 3} \quad \text{(For Landsat 5 and 7)} \qquad (5)$$

On the other hand, band 5 and band 4 of Landsat 8 and 9 represent the reflectance of near-infrared (NIR) and red regions, respectively.

$$\text{NDVI} = \frac{Band\ 5 - Band\ 4}{Band\ 5 + Band\ 4} \quad \text{(For Landsat 8 \& 9)} \qquad (6)$$

Radiance to Brightness Temperature Conversion

By inputting the converted radiant thermal bands into the calculation provided by Zanter (2016), the brightness temperature is determined.

$$T_b = \frac{K_2}{\ln\left(\frac{K_1}{L_\lambda} + 1\right)} \qquad (7)$$

Where, T_b = Top of atmosphere brightness temperature (K)

K_2 = Second calibration constant (K)

K_1 = First calibration constant ($Wm^{-2}sr^{-1}\mu m^{-1}$)

L_γ = Spectral radiance ($Wm^{-2}sr^{-1}\mu m^{-1}$)

The values of the calibration constants are given in (Table 6).

Table 6. Thermal Band Calibration Constants.

Satellite	Constant K_1 ($Wm^{-2}sr^{-1}\mu m^{-1}$)	Constant K_2 (Kelvin)
Landsat 5 TM	607.76	1260.56
Landsat 7 ETM+	666.09	1282.71
Landsat 8 TIRS	774.89	1321.08
Landsat 9 TIRS	799.03	1329.24

Land Surface Emissivity Computation

Land Surface Emissivity (LSE) is the natural materials intrinsic property and is considered a prominent surface attribute. This method can be used to create maps of surface materials for geological studies on Earth as well as other worlds.

The equation used to compute LSE is as follows (Sobrino *et al.*, 2004):

$$\text{LSE} = 0.004 * P_v + 0.986 \qquad (8)$$

Where, P_v = Vegetation proportion

$$P_v = \left[\frac{(NDVI - NDVI_{min})}{(NDVI_{max} - NDVI_{min})}\right]^2 \quad (9)$$

Here, NDVI = Normalized Difference Vegetation Index obtained by previous equation.

$NDVI_{min}$ = Min. value of NDVI

$NDVI_{max}$ = Max. value of NDVI

Retrieval of Land Surface Temperature

The following equation has been employed to compute the Land Surface Temperature (Artis and Carnahan, 1982).

$$LST = \frac{T_b}{1+(\gamma T_b/\alpha)\ln \varepsilon} \quad (10)$$

Where, T_b = At-satellite brightness temperature (K)

γ = Wavelength of emitted radiance (μm)

α = h*c/K = 1.4388 * 10^{-2} m K = 14388 μm K

h = Planck's Constant (6.626 * 10^{-34} J-s)

c = Velocity of light (2.998 * 10^{8} m/s)

K = Boltzmann Constant (1.38 * 10^{-23} J/K)

ε = Land surface emissivity

The values of γ for different Landsat bands are given in (Table 7).

Table 7. Wavelength of emitted radiance used for LST retrieval.

Satellite	Band	Wavelength, γ (μm)
Landsat 4, 5 and 7	6	11.45
Landsat 8	10	10.8
Landsat 9	11	12

Results

Spatial-temporal Distribution of LULC in Bogura District

A systematic analysis was conducted utilizing supervised classification of thematic satellite images from 1993, 2000, 2005, 2010, 2017, and 2023 to examine the changes in land use and land cover (LULC) in the Bogura District (Fig. 3). LULC (Land Use/Land

Cover) Trends reflect a notable increase in settlement areas, which grew from 61.67 km² in 1993 to 625.71 km² in 2023 (Fig. 4). Agricultural land has decreased slightly from 1146.45 km² to 1089.70 km², while vegetation cover has diminished from 1497.06 km² to 831.99 km². The area of waterbodies has remained relatively stable, and bare soil/fallow land has increased from 96.67 km² to 232.30 km², indicating ongoing land degradation or reduced vegetation.

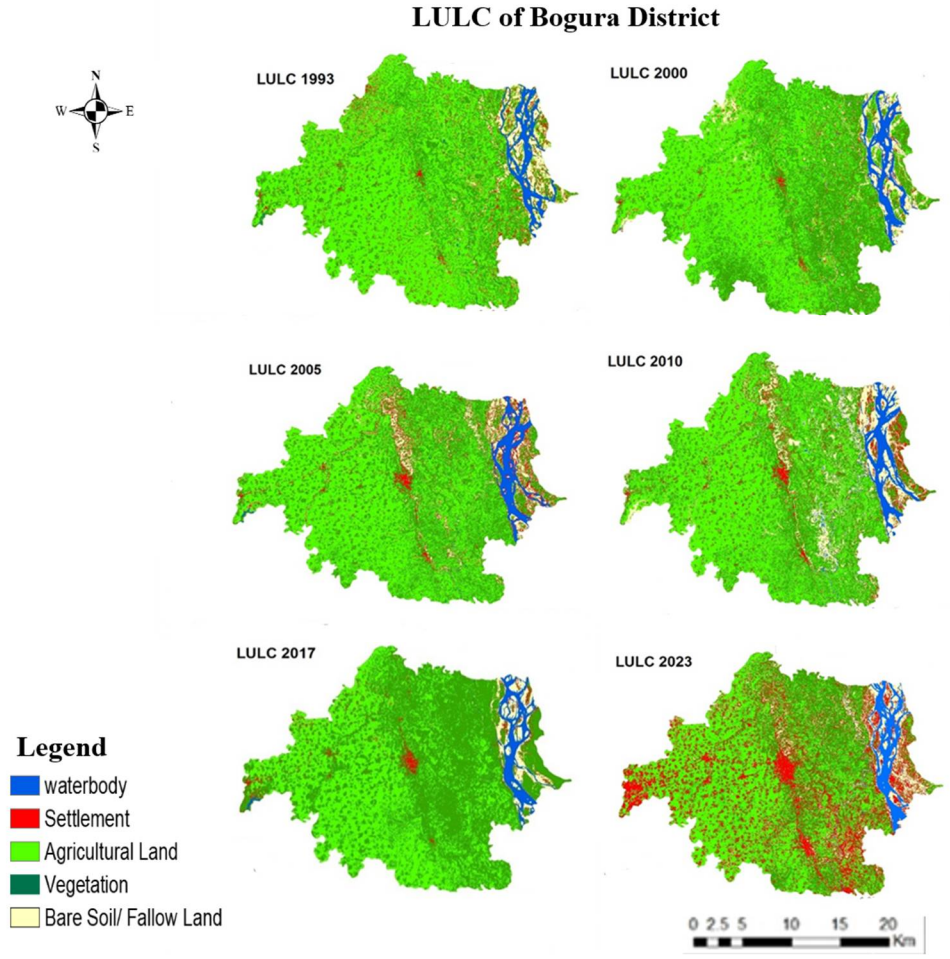

Fig. 3. Supervised classification based spatial distribution of LULC of Bogura District from 1993 to 2023.

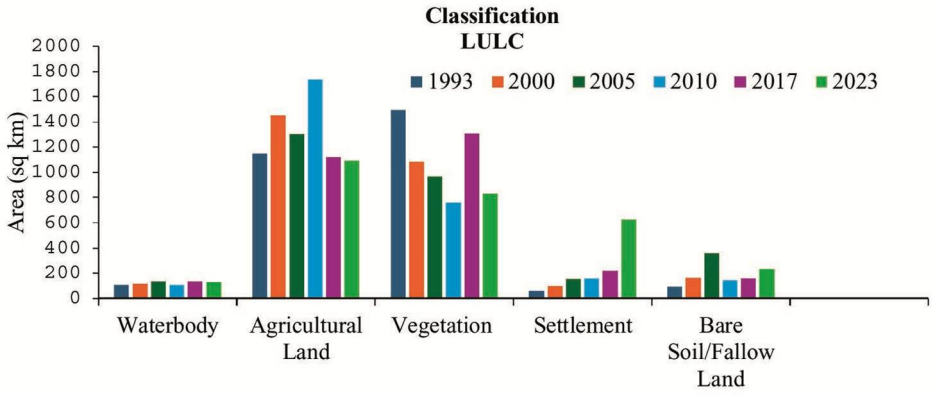

Fig. 4. Graphical representation of LULC calculation from 1993-2023.

Accuracy Assessment result

(Table 8 presents the results from the per-class accuracy assessment for the year 2023. User's accuracy (UA) and producer's accuracy (PA) for most land cover classes ranged between 60% and 88%. The Waterbody class exhibited high accuracy, with UA and PA values of 85% and 88%, respectively, reflecting reliable classification. Similarly, the Settlement class showed strong performance, with UA of 88% and PA of 82%. In contrast, the Agricultural Land and Bare Soil/Fallow Land classes demonstrated lower accuracies, with the lowest PA (62%) observed for Bare Soil/Fallow Land. This is likely due to the spectral similarity between these classes, which introduces misclassification errors. The Vegetation class achieved moderate accuracy, with UA and PA values of 72% and 75%, respectively, indicating some misclassification with other land cover types. Despite these variations, the overall accuracy was 89%, and the Kappa coefficient was 0.815, indicating strong agreement between the classified map and reference data.

Spatial-temporal Distribution of LULC in Bogura Municipality

Bogura Municipality (Bogura Sadar) is in the center of Bogura District and is heavily impacted by urbanization (Fig. 5). The municipality is undergoing massive urbanization development. The Bogura district municipality's settlement area is rapidly expanding. Vegetated and agricultural fields are declining, while habitation and barren lands are growing. Despite fast infrastructure development, the Bogura Sadar or Bogura municipality region faces threats of environmental deterioration and biodiversity loss.

Table 8. Per-class accuracy assessments of multi-temporal for the year 2023.

LULC Class	Samples (n)	User's Accuracy (UA)	Producer's Accuracy (PA)
Waterbody	15	0.85	0.88
Agricultural Land	20	0.65	0.68
Vegetation	20	0.72	0.75
Settlement	20	0.88	0.82
Bare Soil/ Fallow Land	15	0.60	0.62
overall accuracy		0.89	
Kappa coefficient		0.815	

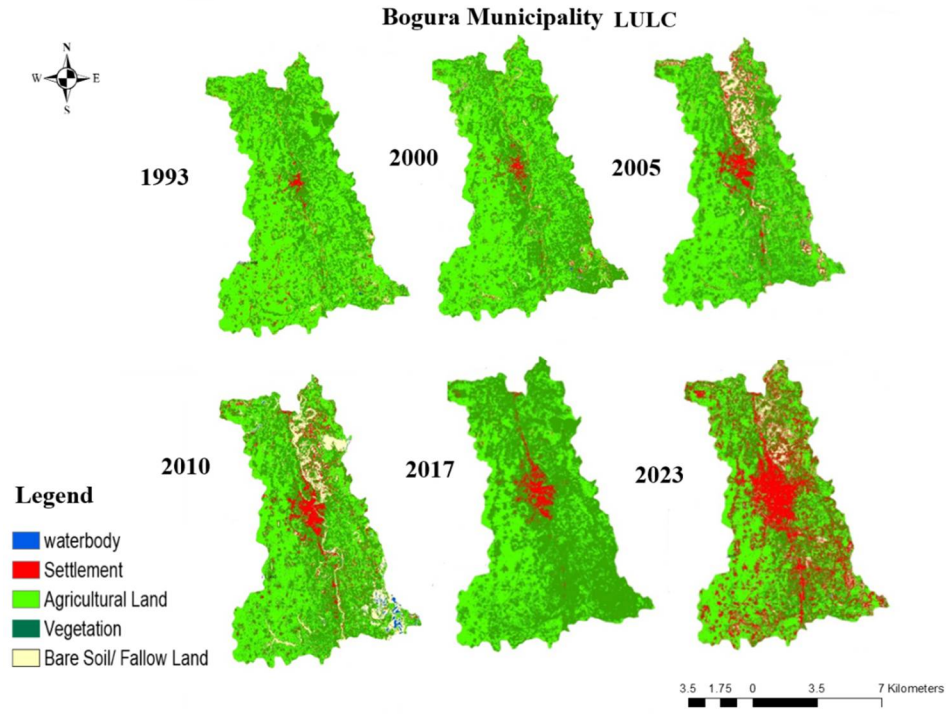

Fig. 5. Spatial Distribution of LULC of Bogura Municipality from 1993 to 2023.

Spatial-temporal Distribution of LST in Bogura District

The land surface temperature areas are classified into five classes which are very low temperature(<24°C), low temperature(24-26°C), moderate temperature(26-28°C), high temperature(28-30°C) and very high temperature (>30°C) covered areas (Fig. 6). The very low temperature category decreased sharply from 2817.96 km² in 1993 to just 61.78 km² in 2023 (Fig. 7). Conversely, areas experiencing low, moderate, high, and very high temperatures have all increased, with the most notable rise in the high temperature category, expanding from 0 km² in 1993 to 140.23 km² in 2023.

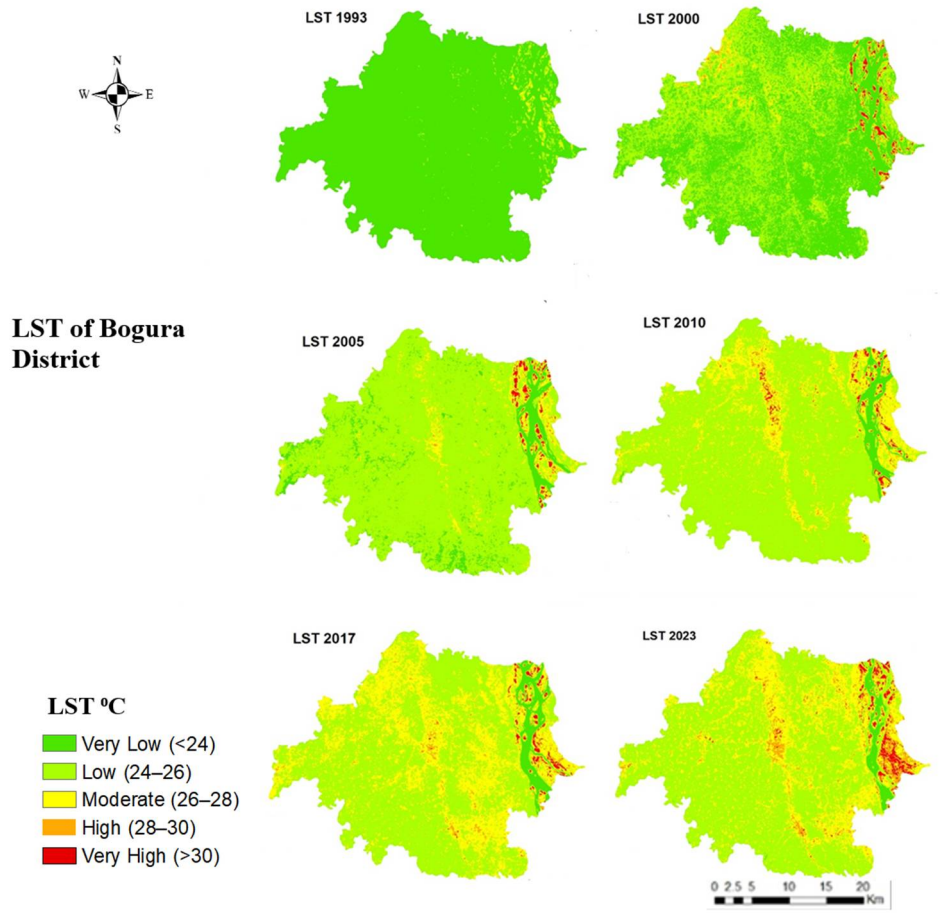

Fig. 6. Spatial Distribution of LST of Bogura District from 1993 to 2023.

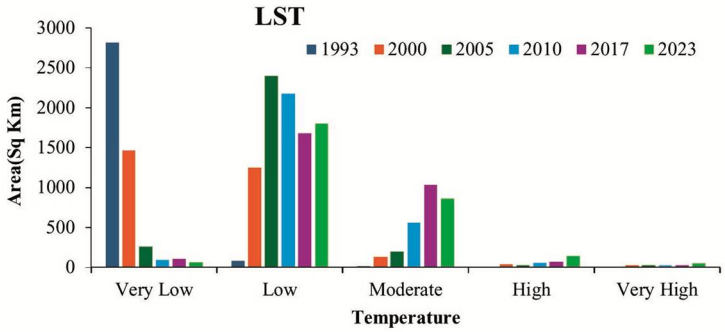

Fig. 7. Graphical representation of LST calculation from 1993-2023.

Spatial-temporal Distribution of NDVI in Bogura District

The NDVI data reveals changes in land cover and vegetation health from 1993 to 2023 (Fig. 8). Waterbody NDVI values declined from 298.86 km² in 1993 to 155.34 km² in 2023, indicating reduced waterbody areas or vegetation around them (Fig. 9). Fallow land

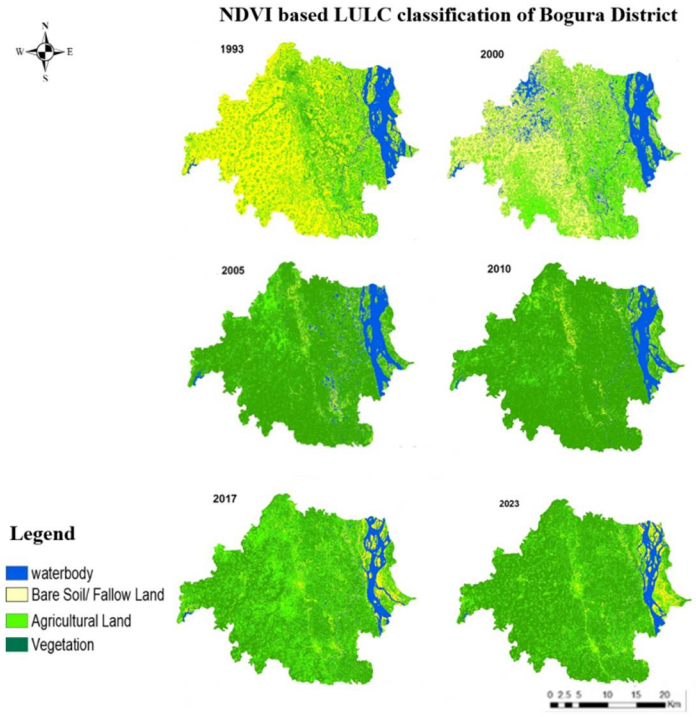

Fig. 8. Spatial Distribution of NDVI based LULC classification of Bogura District from 1993 to 2023.

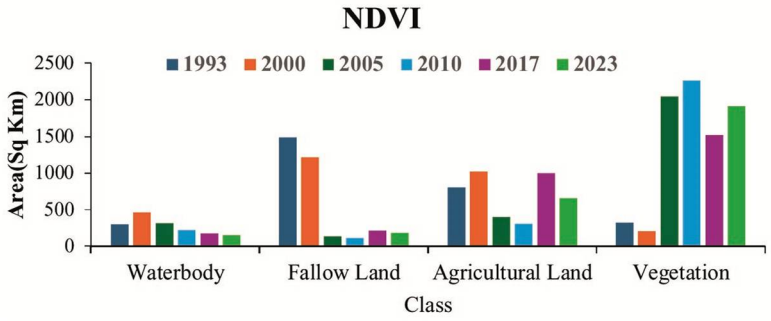

Fig. 9. Graphical representation of NDVI from 1993-2023.

NDVI values fluctuated significantly, dropping from 1489.71 km² in 1993 to 182.85 km² by 2023, reflecting a decrease in fallow land or vegetation changes. Agricultural land NDVI values increased from 802.85 km² in 1993 to 1003.45 km² in 2017 but then decreased to 657.90 km² in 2023, suggesting variations in agricultural practices. Vegetation NDVI values generally rose from 320.39 km² in 1993 to a peak of 2263.31 km² in 2010 before slightly decreasing to 1915.71 km² in 2023, indicating overall improved vegetation health with some fluctuations.

Discussion

The analysis of spatiotemporal changes in Bogura District from 1993 to 2023 reveals significant shifts in land use, land surface temperature (LST), and vegetation cover. The NDVI analysis highlights a substantial increase in vegetation cover, rising from 320.39 km² in 1993 to 1915.71 km² in 2023. This indicates overall improved vegetation health, although the increase in vegetation is somewhat counterbalanced by the notable decline in other land cover types. Waterbodies have decreased dramatically from 298.86 km² to 155.34 km², and fallow land has sharply reduced from 1489.71 km² to 182.85 km². Agricultural land has also seen a reduction, from 802.85 km² to 657.90 km², suggesting shifts in land use and potential impacts on local ecosystems.

The LST data reveals a significant shift towards higher temperature categories. The area classified under very low temperatures has decreased sharply from 2817.96 km² in 1993 to just 61.78 km² in 2023. Conversely, areas experiencing low, moderate, high, and very high temperatures have all increased, with the most notable rise observed in the high temperature category, expanding from 0 km² in 1993 to 140.23 km² in 2023. This shift reflects the intensifying urban heat island (UHI) effect driven by increased urbanization.

Land Use/Land Cover (LULC) trends further underscore the impact of urbanization. Settlement areas have expanded significantly from 61.67 km² in 1993 to 625.71 km² in 2023, highlighting rapid urban growth. Concurrently, agricultural land has decreased slightly from 1146.45 km² to 1089.70 km², while vegetation cover has diminished from 1497.06 km² to 831.99 km². The area of waterbodies has remained relatively stable, but bare soil and fallow land have increased from 96.67 km² to 232.30 km², indicating ongoing land degradation or reduced vegetation.

The strengths of this study lie in its comprehensive analysis using multispectral satellite images, which provides a detailed understanding of land use dynamics and their effects on surface temperatures. However, the study's reliance on satellite data alone may not capture all local variations, and integrating field surveys could enhance the accuracy of the findings.

This research is crucial for addressing the adverse impacts of urbanization and climate change. By identifying the key areas of change and their effects on temperature and vegetation, the study supports the development of strategies for sustainable urban planning and climate resilience. It provides a framework for mitigating the urban heat island effect and guiding efforts to balance urban growth with environmental conservation.

Conclusion

The strong link between land use-land cover (LULC) changes, Normalized Difference Vegetation Index (NDVI) variations, and land surface temperature (LST) help to understand the development of heat islands in Bogura District. Rapid urbanization has led to significant increases in settlement areas and surface temperatures, intensifying the urban heat island (UHI) effect. As urban areas expand, they replace vegetation and water bodies with impervious surfaces, contributing to higher LST and reduced NDVI values. The decline in fallow and agricultural lands, driven by growing food demands and urban sprawl, exacerbates habitat loss and environmental degradation. The findings underscore the urgent need for sustainable development strategies to mitigate the UHI effect, preserve biodiversity, and balance urban growth with ecological conservation.

Acknowledgement

Authors are gratefully acknowledged the USGS archive to provide satellite images with free of cost.

References

Ahmed, B., I. Kelman, M. Kamruzzaman, H. Mohiuddin, M.M. Rahman, A. Das and M. Shamsudduha. 2019. Indigenous people's responses to drought in northwest Bangladesh. *Environ. Develop.* **29**: 55-66.

Artis, D.A. and W.H. Carnahan. 1982. Survey of emissivity variability in thermography of urban areas. *Remote Sens. Environ.* **12**(4): 313-329.

Bangladesh Bureau of Statistics (BBS). 2022. *Population and housing census 2022*.

Bangladesh Meteorological Department (BMD). 2021. *Monthly maximum temperature*. Retrieved from http://live3.bmd.gov.bd/p/Monthly-Maximum-Temperature/ (Accessed September 6, 2021).

Borges, C.K., R.M. de Medeiros, R.E. Ribeiro, É. G. dos Santos, R. G. Carneiro and C.A. dos Santos. 2016. Study of biophysical parameters using remote sensing techniques to Quixeré-CE region. *J. Hyperspec. Remote Sens.* **6**(6): 283-294.

Ding, H. and W. Shi 2013. Land-use/land-cover change and its influence on surface temperature: A case study in Beijing City. *Inter. J. Remote Sens.* **34**(15): 5503-5517.

Jie, B., L. Shaomin and H. Guang. 2008. Inversion and verification of land surface temperature with remote sensing TM/ETM+ data. *Transactions of the Chinese Society of Agricultural Engineering*, **2008**(9).

Kustas, W.P. and J.M. Norman. 1996. Use of remote sensing for evapotranspiration monitoring over land surfaces. *Hydrol. Sci. J.* **41**(4): 495-516.

Luck, M. and J. Wu. 2002. A gradient analysis of urban landscape pattern: A case study from the Phoenix metropolitan region, Arizona, USA. *Landscape Ecol.* **17**(4): 327-339.

Pielke, R.A. 2005. Land use and climate change. *Science*, **310**(5754): 1625-1626.

Ramachandra, T.V., B.H. Aithal and D. Sanna. 2012. Land surface temperature analysis in an urbanizing landscape through multi-resolution data. *Research & Reviews: Journal of Space Science & Technology*, **1**(1): 1-10.

Rouse Jr, J., R.H. Haas, J. A. Schell and D.W. Deering. 1974. Monitoring vegetation systems in the Great Plains with ERTS.

Sobrino, J.A., L. Paolini, F.Grings, J.C. Jiménez-Muñoz and H. Karszenbaum. 2006. Radiometric correction effects in Landsat multi-date/multi-sensor change detection studies. *Inter. J. Remote Sens.* **27**(4): 685-704.

Voogt, J.A. and T.R. Oke, 2003. Thermal remote sensing of urban climates. *Remote Sens. Environ.* **86**(3): 370-384.

Walawender, J. P., M. Szymanowski, M.J. Hajto, and A. Bokwa. 2014. Land surface temperature patterns in the urban agglomeration of Krakow (Poland) derived from Landsat-7/ETM+ data. *Pure Appl. Geophy.***171**(6): 913-940.

Weng, Q. (2001). A remote sensing–GIS evaluation of urban expansion and its impact on surface temperature in the Zhujiang Delta, China. *Inter. J. Remote Sens.* **22**(10): 1999-2014.

Xie, Q., and Z. Zhou. 2015. Impact of urbanization on urban heat island effect based on TM imagery in Wuhan, China. *Environ. Eng. Manage. J.* **14**(3): 647-655.

Zanter, K. 2016. *Landsat 8 (L8) data users handbook. Landsat Science Official Website, 33*.

(Revised copy received on 18/03/2025)